Search for X-Ray Emission Associated with the Shapley Supercluster with *Suzaku*

Ikuyuki Mitsuishi[1], Anjali Gupta[2], Noriko Y. Yamasaki[1], Yoh Takei[1], Takaya Ohashi[3], Kosuke Sato[4], Massimiliano Galeazzi[2], J. Patrick Henry[5], and Richard L. Kelley[6]

[1]*Institute of Space and Astronautical Science, Japan Aerospace Exploration Agency (ISAS/JAXA), 3-1-1 Yoshinodai, Chuo-ku Sagamihara, Kanagawa, 252-5210*
mitsuisi@astro.isas.jaxa.jp

[2]*Physics Department, University of Miami, 1320 Campo Sano Drive Coral Gables, FL 33146, USA*

[3]*Department of Physics, Tokyo Metropolitan University, 1-1 Minami-Osawa, Hachioji, Tokyo, 192-0397*

[4]*Department of Physics, Tokyo University of Science, 1-3 Kagurazaka, Shinjyuku-ku, Tokyo 162-8601*

[5]*Institute for Astronomy, University of Hawaii, 2680 Woodlawn Drive, Honolulu, HI 96822, USA*

[6]*NASA/Goddard Space Flight Center, Greenbelt, MD 20771, USA*

(Received 2011 May 31; accepted 2011 September 14)

Abstract

Suzaku performed observations of 3 regions in and around the Shapley supercluster: a region located between A3558 and A3556, at ~ 0.9 times the virial radii of both clusters, and two other regions at 1° and 4° away from the first pointing. The 4°-offset observation was used to evaluate the Galactic foreground emission. We did not detect significant redshifted Oxygen emission lines (O VII and O VIII) in the spectra of all three pointings, after subtracting the contribution of foreground and background emission. An upper limit for the redshifted O VIII Kα line intensity of the warm-hot intergalactic medium (WHIM) is 1.5×10^{-7} photons s^{-1} cm^{-2} arcmin^{-2}, which corresponds to an overdensity of $\sim 380\ (Z/0.1\ Z_{\odot})^{-1/2}(L/3\ \mathrm{Mpc})^{-1/2}$, assuming $T = 3 \times 10^6$ K. We found excess continuum emission in the 1°-offset and on-filament regions, represented by thermal models with $kT \sim 1$ keV and ~ 2 keV, respectively. The redshifts of both 0 and that of the supercluster (0.048) are consistent with the observed spectra. The ~ 1 keV emission can be also fitted with Ne-rich Galactic (zero redshift) thin thermal emission. Radial intensity profile of 2 keV component suggests contribution from A3558 and A3556, but with significant steepening of the intensity slope in the outer region of A3558. Finally, we summarized the previous *Suzaku* search for the WHIM and discussed the feasibility of constraining the WHIM. An overdensity of < 400 can be detectable using O VII and O VIII emission lines in a range of $1.4 \times 10^6\ \mathrm{K} < T < 5 \times 10^6$ K or a continuum emission in a relatively high temperature range $T > 5 \times 10^6$ K with the *Suzaku* XIS. The non detection with *Suzaku* suggests that typical line-of-sight average overdensity is < 400.

Key words: X-ray, cluster, supercluster, WHIM

1. Introduction

History of the Universe has been revealed little by little but constantly. Some fundamental mysteries are, however, remaining. One of these unresolved questions is the so-called "missing baryon" problem. More than half of the total baryonic matter in the current epoch (z<1) has not been detected, and is known as the "missing baryons". Cosmological hydrodynamic simulations (e.g., Cen & Ostriker 1999; Davé et al. 2001) predict that most of missing baryons are expected to be in the phase of warm-hot intergalactic medium (WHIM), a plasma existing along filamentary large-scale structures connecting clusters of galaxies. The WHIM may be detected in UV and X-rays, since its expected temperature is 10^5 to 10^7 K. However, due to its low density and low temperature on the order of 10^{-5} to 10^{-3} cm^{-3} and 10^5 to 10^7 K, technically, it is difficult to achieve a sufficient sensitivity, especially in the X-ray energy.

Many observational progresses on the WHIM has been recently reported. In the UV band, O VI absorption lines (λ = 1032, 1038 Å) have been detected along the lines of sight to ~ 50 AGN (e.g., Danforth & Shull 2005; Danforth & Shull 2008; Tripp et al. 2008), by *FUSE* and Hubble Space Telescope. If we assume all the observed O VI lines are produced by the WHIM, then the O VI can probe 7–10 % of the baryons (Danforth & Shull 2005; Tripp et al. 2006; Danforth 2009). With the inclusion of the thermally broadened Lyα absorbers (BLAs) recently observed by Danforth et al. (2010) and Narayanan et al. (2010a); Narayanan et al. (2010b), these estimates are boosted up by a factor of ~2, i.e., UV observations are capable of probing ~20% of the baryons in the local universe (Danforth et al. 2010). In X-ray band, there are many observations to investigate the absorption lines from highly ionized ions, but they lead to only several marginal ($< 4\sigma$) detection of absorption lines associated with dense parts of large-scale structures (Fujimoto et al. 2004; Takei et al. 2007a; Buote et al. 2009; Fang et al. 2010). Two examples of the possible WHIM signal are an excess X-ray continuum (modeled as T =0.9 keV plasma) emission in a filamentary region between A222 and A223 by XMM-Newton (Werner et al. 2008) and a signature on the angular correlation of diffuse X-ray emission in six accumulated intergalactic filaments (Galeazzi et al.

2009). Emission lines of O VII and O VIII in X-ray spectra can also be used as a signature of the WHIM. However, it is challenging for present instruments because of the low intensity of the thin plasma and because of the difficulty of distinguishing it from the soft Galactic emission. Nevertheless, thanks to the good sensitivity and line spread function at the lower energy below 1 keV of the XIS (X-ray Imaging Spectrometer; Koyama et al. 2007) detectors on board *Suzaku* (Mitsuda et al. 2007), the good constrains on the WHIM properties has been obtained (Takei et al. 2007b; Sato et al. 2010). *Suzaku* XIS is also used as a powerful tool to extend the ICM study to out skirt regions around virial radii (Bautz et al. 2009; George et al 2009; Kawaharada et al. 2010; Hoshino et al. 2010; Simionescu et al. 2011).

In this paper, we report on observations in a supercluste as a target to search for the WHIM emission. Supercluster are thought to be promising targets because they are know as the most largest and densest structures associated with th large scale structures inducing a WHIM concentration and be cause the faint WHIM emission is accumulated along the line of-sight depth of the order of several Mpc or more. Amon them, we focused on the Shapley supercluster (z = 0.048) us ing *Suzaku*.

Throughout this paper, we adopt $H_0 = 73$ km s^{-1} Mpc^{-1}, Ω_M = 0.73 and Ω_Λ = 0.27, which corresponds to 57 kpc arcmin^{-} at the redshift of 0.048. Unless otherwise specified, all error are at 90 % confidence level.

2. Observations & Data Reduction

2.1. *Observations*

Three pointings in and around the Shapley supercluster were carried out with *Suzaku* in July 2008 (PI: Ohashi & Galeazzi). The Shapley supercluster is one of promising candidates to search for an emission from the WHIM because this is one of the largest (Fabian 1991; Jaaniste et al. 1998) and most massive (Muñoz & Loeb 2008) structures in the local Universe on the order of several 10 Mpc and 10^{16} $M_\odot$, respectively. Actually, ROSAT detected an excess emission between 0.5 and 2 keV in the Shapley supercluster above the surrounding fields (Kull & Böhringer 1999), which may indicate the emission of WHIM origin. Thus we observed the same region between A3556 ($kT \sim 3.2$ keV, Akimoto et al. 2003) and A3558 ($kT \sim 5.6$ keV, Akimoto et al. 2003), located close to the center of the Shapley supercluster (hereafter we call the field as ON-FILAMENT). In addition, two offset regions at $\sim 1°$ (hereafter OFFSET-1deg) and $\sim 4°$ (OFFSET-4deg) from the ON-FILAMENT region were observed to constrain the foreground emission around the supercluster. Observed regions are shown in Figure 1 with the distribution of galaxies whose redshifts are known with the NASA Extragalactic Database (NED) and in the range of $0.046 < z < 0.050$. This redshift range includes the nearby clusters A3556 ($z = 0.0479$), A3558 ($z = 0.048$) and A3562 ($z = 0.049$) in the Shapley supercluster, and the corresponding velocity width is ~ 600 km s^{-1} at $z = 0.048$. It is not completely surveyed, and the magnitude is ranging from 13.5 to 20.3, 14.2 to 17.2 in R-band, 14.0 to 15.5 in I-band and 12.6 to 20.4 in V-band respectively. The sequence numbers, observation dates, pointing directions, exposure times and the hydrogen column densities are summarized in Table 1. We confirmed that the difference between the Galactic hydrogen column density by Kalberla et al. (2005) from the LAB survey and Dickey & Lockman (1990) was only less than 10 % on the order of several 10^{20} cm^{-2}, which leads to a systematic error of <3 % for the best-fit values in the analysis. This was smaller than the statistical errors. In the spectral fitting shown in this paper, we always fixed the N_H value at the LAB survey values because of its better angular resolution.

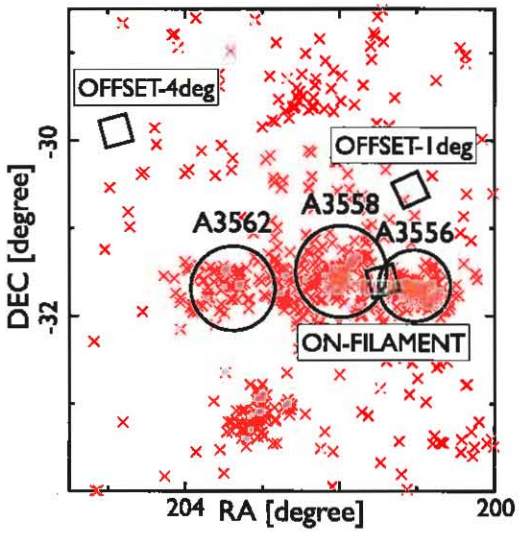

Fig. 1. The distribution of galaxies with known redshifts (red crosses) in the range of $0.046 < z < 0.050$. Circles indicate the virial radius of each cluster. The virial radius of A3558 and A3562 are adopted in Rossetti & Molendi (2010) and A3556 is calculated using the equation (1) in Hoshino et al. (2010). Three squares show the fields of view of *Suzaku XIS* in the OFFSET-1deg, OFFSET-4deg and ON-FILAMENT pointings.

2.2. *Data Reduction*

In this work, we analyzed only the XIS data. The data reduction and analysis were carried out with HEAsoft version 6.11 and XSPEC 12.7.0 with AtomDB ver.2.0.1. We produced the redistribution matrix files (RMFs) by xisrmfgen ftool, in which a degradation of energy resolution and its position dependence are included. We also prepared ancillary response files (ARFs) using xissimarfgen ftool (Ishisaki et al. 2007). An input image to xissimarfgen is a uniform circle of a radius of 20′, except for ARFs for point source candidates. For the ARFs of the point source candidates, we simply assumed point source images at the source positions in the sky. As a systematic uncertainty in the thickness of the XIS optical blocking filter, we considered ±20%. With these uncertainties, we examined the significance of the excess component as described in § 3. To reproduce the non X-ray background (NXB) component, we utilized an accumulated dark Earth database with the "xisnxbgen" ftools task (Tawa et al. 2008).

In addition to standard data processing (e.g. ELV > 5 and DYE_ELV > 20), we examined if additional filtering was necessary. Firstly, we checked a contamination of a fluorescent scattering of the neutral oxygen line from the atmosphere of

Table 1. Observation log

		ON-FILAMENT	OFFSET-1deg	OFFSET-4deg
Sequence number		803072010	803068010	803021010
Obs date		2008-07-10 to 2008-07-13	2008-07-19 to 2008-07-23	2008-07-18 to 2008-07-19
$(\alpha_{2000},\delta_{2000})$	degree	(201.5, -31.6)	(201.1, -30.6)	(204.9, -29.9)
(ℓ, b)	degree	(311.4, 30.7)	(311.3, 31.8)	(315.2, 31.8)
Exposure	ks	30.2*	143	47.2
N_H	cm^{-2}	4.15×10^{20}	4.78×10^{20}	3.98×10^{20}

* After the COR screening as described.

the Earth. The flux of the line is characterized by a total column density of neutral oxygen atoms and molecules in a sun-lit atmosphere (e.g., Smith et al. (2007)). We adopted a column density threshold of 10^{14} cm^{-2} and compared the spectra including and excluding the duration in which the column density of sun-lit atmosphere is above the threshold. The two spectra were consistent with each other within statistical errors.

Secondly, we examined contaminant emission from the solar wind charge exchange (SWCX) near the Earth, which is caused by ions in the Solar wind penetrating into the geomagnetic field and atmospheric neutral hydrogen (Fujimoto et al. 2007; Gupta et al. 2009; Yoshino et al. 2009). We applied the same screening procedure as described in Hagihara et al. 2010. The parameters we considered were a proton flux from the sun and an Earth-to-magnetopause distance in the line of sight of *Suzaku*. The higher proton flux indicates higher ion flux that produces a contamination of specific lines through the CX process as describe in Ezoe et al. (2010). We take 4×10^8 cm^{-2} s^{-1} as a threshold of proton flux. During times with the smaller Earth-to-magnetopause distance, more larger charged particles are able to reach the vicinity of the Earth, which results in the larger contamination (Fujimoto et al. 2007). A threshold of five times the Earth radius away from the Earth center is adopted. Then we compared the screened spectra with the non-screened one. The two spectra turned out to be consistent with each other within the statistical errors. Therefore, we did not remove these durations but utilized all the observed data.

Thirdly, we performed a data screening with the cut-off-rigidity (COR) of the Earth's magnetic field for the ON-FILAMENT observation, because we found discrepancy between FI and BI sensors in the ON-FILAMENT spectra in 2.0–5.0 keV, which may be due to the fluctuation of the detector background. The COR value corresponds to the threshold momentum preventing a charged particle from reaching the surface of the Earth. A particle (e.g., cosmic rays) whose momentum is smaller than the COR value is screened by the Earth's magnetic field. When COR is small, more particles with smaller momentum can reach to the detectors, which leads to a higher particle background and larger systematic errors (Tawa et al. 2008). The screening was done based on COR2 parameter (Tawa et al. 2008). The spectra from different sensors became consistent with each other within the statistical errors if the selection of COR2 > 12 GV was applied. For OFFSET-1deg and OFFSET-4deg regions, we did not impose this screening since no discrepancy was found between the results with and without the COR screening.

After the above screenings, we removed point source candidates in each region with a radius of 1′.2 to 2′ depending on the source intensity. We picked up point sources in the XIS1 image in 0.4–2.0 keV, based on wavelet algorithm (by a CIAO tool wavdetect) for point-like sources. We also carried out visual inspection and extracted somewhat diffuse-like sources which were not effectively detected with this algorithm. As a result, the numbers of point source candidates found are 5, 8 and 7 for the ON-FILAMENT, OFFSET-1deg and OFFSET-4deg regions, respectively.

Then, in order to determine the detection limit, we evaluated NXB-subtracted fluxes of these sources. The detection limit will be utilized to estimate the flux and expected fluctuation of the CXB (i.e., unresolved point sources) in §3.2. The spectrum of each point source was produced, followed by subtraction of the NXB spectrum at the same detector region. The NXB spectrum was re-normalized by adjusting the count rate in 10–15 keV to the source intensity. The re-normalization is applied to the whole spectrum. Note that the effective area of XRT in 10–15 keV is so small that all the counts in the source data can be considered as the NXB contribution. The re-normalization factor is less than 5% in most cases. To improve the spectral fit, we adopted this re-normalization to the NXB spectrum. However, the best-fit parameters did not change significantly even without this process. Next, we fitted the NXB-subtracted spectra of point source candidates in 2.0–10.0 keV with an absorbed power-law model. The source fluxes in 2.0–10.0 keV are larger than 1.2×10^{-13} ergs cm^{-2} s^{-1} for the ON-FILAMENT, 2.8×10^{-14} ergs cm^{-2} s^{-1} for the OFFSET-1deg and 4.1×10^{-14} ergs cm^{-2} s^{-1} for the OFFSET-4deg. XIS1 images in 0.4–2.0 keV from which the regions of point source candidates are excluded are shown in Figure 2.

We removed cal sources by status filter in XSELECT located in the edge of a CCD detector in order to analyze the data in the energy band above 5 keV. We fitted the spectra of the FI and BI sensors simultaneously, but in different energy ranges which were 0.4-8.0 keV for the BI and 0.5-8.0 keV for the FI, respectively, after the above data reduction.

3. Analysis & Results

3.1. Background/foreground Emission Analysis

Since the expected WHIM emission is soft and weak, a careful treatment of the background and foreground emission is mandatory. Thus firstly, we analyzed the data in the offset regions (OFFSET-1deg and OFFSET-4deg). We fitted the spectra with a sum of (1) an unabsorbed thin thermal collisionally-ionized equilibrium (CIE) plasma, (2) an absorbed thin ther-

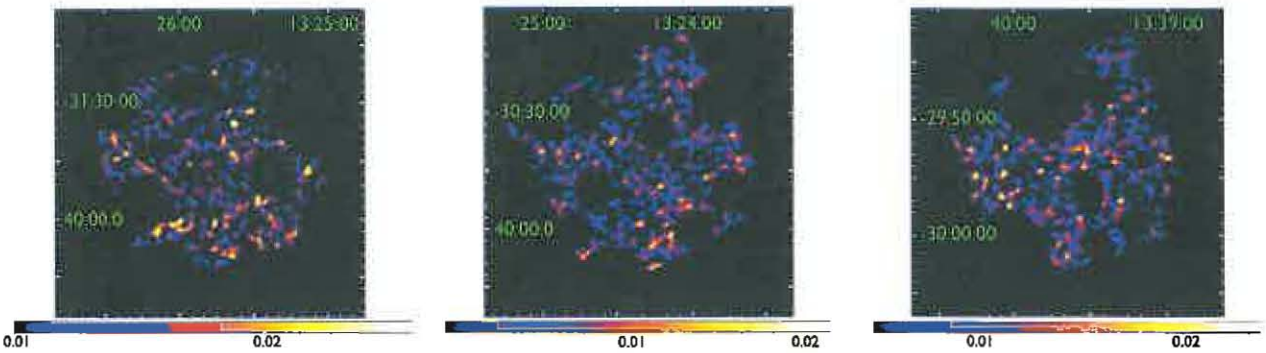

Fig. 2. The XIS1 images for the ON-FILAMENT (left), OFFSET-1deg (middle) and OFFSET-4deg (right) regions. The energy range is 0.4–2.0 keV in units of cts ks^{-1} (64 pixel)$^{-1}$. The images are smoothed with a kernel of $\sigma = 8.3$ arcsec and the scale is logarithmic. Vignetting and background are not corrected for and cal sources are removed. The FOV of *Suzaku* XIS is $18' \times 18'$.

mal CIE plasma and (3) an absorbed power law, modeled as Lumb et al. (2002). These first two plasmas represent contributions from the local emission (SWCX and Local Hot Bubble: LHB) and Galactic halo (MWH: Milky Way Halo), respectively. The abundance is set to 1 solar for both models. The component (3) corresponds to the accumulation of unresolved extragalactic point sources (cosmic X-ray background: CXB), which is described by an absorbed power-law model with a photon index of 1.4 in Kushino et al. 2002. In summary, we used the following models: $apec_1$ + $phabs\times$ ($apec_2$+ *power-law*). These three components are known as the typical X-ray background and foreground emission. The best-fit parameters and spectra are shown in Table 2 (in columns labeled as Nominal) and in Figure 3. The temperatures of the two thermal plasmas (~ 0.1 keV and ~ 0.25 keV in both regions) are typical values reported in Yoshino et al. (2009), which studied 14 *Suzaku* spectra in the blank sky fields. Kushino et al. 2002 discussed the CXB surface brightness using a $\log N - \log S$ relation. According to the relation and the present detection limits in the two regions, the normalizations are expected to be 6.8 and 7.3 photons s^{-1} cm^{-2} sr^{-1} keV^{-1} at 1 keV, in OFFSET-1deg and OFFSET-4deg regions, respectively. These values are consistent with the observed ones.

For each region, we evaluated line centers and surface brightnesses of O VII Kα and O VIII Kα emission lines. In the best-fit model of each region, we replaced the *apec* model with a *vapec* model whose Oxygen abundance was set to be 0 and added two Gaussian lines. These lines represented O VII and O VIII emission lines. The abundances of other elements were fixed to be 1 solar, and temperatures of the vapec components were fixed to the best-fit values for the individual fits. The line centers and the surface brightnesses were derived from these spectral fits, and the results are summarized in Table 3. The line centers are consistent with zero redshift within statical errors and within the typical energy determination accuracy of XIS. The implication for the line intensity will be discussed in § 3.3.

We also looked into the possible excess continuum in both the spectra. While addition of another thermal model did not improve the fit for OFFSET-4deg spectrum, it slightly improved the fit for the OFFSET-1deg one. This is shown in the column $3T$ ($z = 0$) of Table 2. The temperature of the additional component is ~0.9 keV. A similar improvement was obtained by adding a thermal emission with the supercluster redshift ($3T$ ($z = 0.048$) of Table 2). Since this excess component is apparently peaked around 0.9 keV, we also tried a model with different metal abundance. Since Ne lines are concentrated in this energy, we tried to fit with a vapec model for the MWH component with variable Ne abundance and other elements fixed at 1 solar done in Yoshino et al. (2009). As shown in the column (Z_{Ne} free of Table 2), this model also showed an equally good fit. The spectra fitted with these models are shown in Figure 3 and 4. A Ne-rich or higher temperature (~0.7 keV) Galactic emission is reported in some of high-latitude fields, but not the same as the OFFSET-1deg region, studied in Yoshino et al. (2009), which shows that we can not deny the possibility of the Galactic emission origin.

3.2. *Emission Analysis in the ON-FILAMENT region*

In this section, we examined whether the ON-FILAMENT can be explained by a normal emission model (LHB+SWCX, MWH and CXB) as is the case of the OFFSET-4deg region or any excess component is needed as is the case of the OFFSET-1deg region. As the starting point, we simply compared the obtained spectrum between offset regions and the ON-FILAMENT region by fixing all parameters to the best fit values obtained in the OFFSET-1deg (Z_{Ne} free in Table 2) and the OFFSET-4deg regions, respectively as shown in Figure 5. We found that large residuals remained not only in a soft band below 1 keV where the Galactic emission is responsible for but also in a hard band above 1 keV.

We evaluated the excess emission in the ON-FILAMENT region in comparison with the offset region in consideration with field-to-field variation of the background intensity. The spectra of the ON-FILAMENT region are fitted simultaneously with the background parameters linked together. We let the normalization of the two Galactic thermal components vary with the same scaling factor (f), and normalization of the CXB component was set as a free parameter independent of f.

Firstly, the OFFSET-4deg region was used as a background spectrum because the OFFSET-4deg region was fitted well with the typical model for the blank X-ray sky as described in the

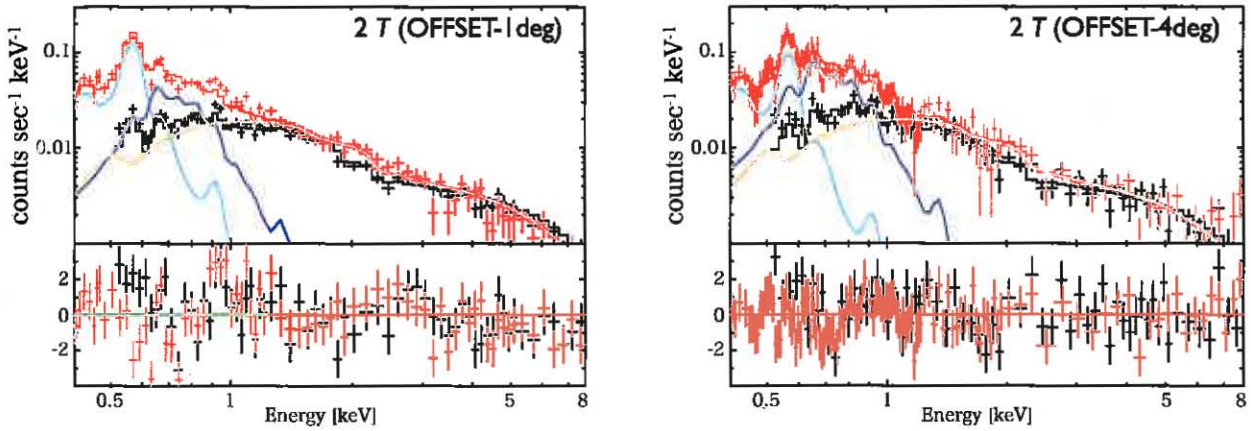

Fig. 3. Spectra in 0.4–8.0 keV of the OFFSET-1deg (left) and the OFFSET-4deg (right) regions. Red and black data are for the BI and FI sensors, respectively. The lines show the best-fit model that consists of (1) *apec*$_{\rm LHB}$ (cyan), (2) *phabs*× *apec*$_{\rm MWH}$ (blue), and (3) *phabs*× *power-law* (orange). The components (1), (2), and (3) correspond to LHB+SWCX, MWH and CXB, respectively. The photon index of the CXB is fixed to be 1.4.

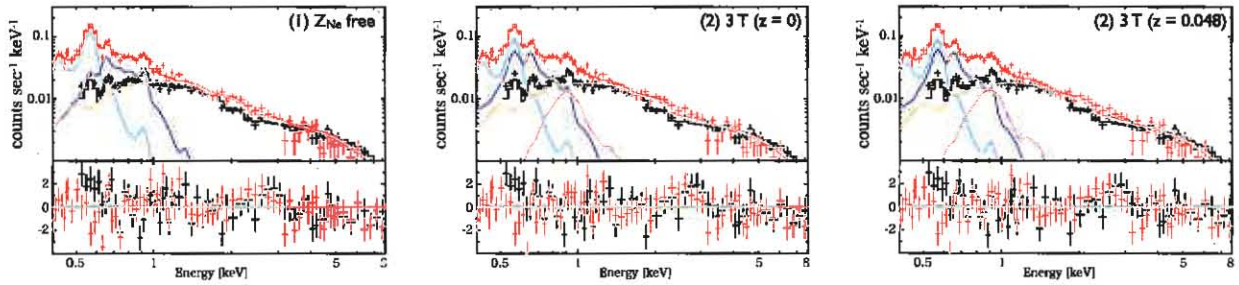

Fig. 4. Spectral fits for the OFFSET-1deg data in 0.4–8.0 keV with different models. Red and black data are for the BI and FI sensors, respectively. (left) (1) + (2) + (3) but Ne abundance of the MWH was set to be free to model the residual at around 0.9 keV. (middle) (1) + (2) + (3) + one more higher temperature plasma at redshift 0. (right) (1) + (2) + (3) + one more higher temperature plasma at the redshift of the supercluster. See caption of Fig. 3 about the components (1), (2) and (3). Cyan, blue, orange and magenta lines indiate LHB+SWCX, MWH, CXB, and the additional higher temperature plasma, respectively. The photon index of the CXB is fixed to be 1.4.

previous section. As indicated in Figure 6 and Table 4, the energy spectrum of the ON-FILAMENT region below 1 keV is well represented by the typical Galactic emission by the same Galactic emission as OFFSET-4deg with a scaling factor f = 0.98±0.07. The CXB surface brightness was 13.3 photons s^{-1} cm^{-2} keV^{-1} at 1 keV, which is significantly larger than the expected value from the detection limit of removed point sources (8.3 photons s^{-1} cm^{-2} keV^{-1} at 1 keV) if we estimate according to Hoshino et al. (2010). Note that the fluctuation can be estimated by the same way described in Hoshino et al. (2010) from Ginga observations (Hayashida et al. 1989) to be ~9 % considering the Poisson noise of the number of sources in the FOV under the detection limit. This suggests that some sort of continuum emission may exist in addition to the CXB in the energy range above 1 keV. We thus added one more thermal plasma to evaluate the excess continuum at a redshift of either 0 or that of the supercluster, with the abundance of the additional plasma fixed to the solar value. The 3T model improved the fit compared to the 2T model. The difference in the goodness of the fit between the two redshifts are small. Hence we cannot statistically determine the origin of the emission. These 3T fit results are shown and summarized in Figure 6 and Table 4. However, the CXB level is still high and a normalization of the CXB and a temperature of the additional plasma are correlated strongly. If we restrict the normalization of the CXB up to 10.5 photons s^{-1} cm^{-2} keV^{-1} sr^{-1} at 1 keV corresponding to 3 σ upper limit of the expected value in the ON-FILAMENT region, the temperature of the additional plasma in (z = 0, Z = 1 $Z_\odot$) model of Table 4 goes up to $2.1^{+0.8}_{-0.2}$ keV and $10.2^{+0.4}_{-0.2}$ in the normalization. Thus a temperature of the additional plasma can be higher. The fit was slightly improved if we fix the abundance of the additional thermal component at 0.3 solar. The best-fit temperature and normalization were higher in this case.

Next, to evaluate a systematic error caused by the difference of a selected background region, the OFFSET-1deg region was also used as a background for the ON-FILAMENT region. The same analysis was performed as the OFFSET-4deg region and spectra and the best fit values are shown and summarized in Figure 7 and Table 5. As Galactic emission models, we tried both the two acceptable models denoted $Z_{\rm Ne}$ free and 3 T (z = 0) in Table 2. Here, we showed only results of the $Z_{\rm Ne}$ free model because we confirmed that resulting parameters for the excess emission in the ON-FILAMENT spectrum were consistent with each other within the statistical errors. Resultant parameters for the additional plasma are also consistent with each other between the OFFSET-1deg and the OFFSET-4deg. It means that this kind of systematic error does not affect our results discussed in later section.

Table 2. Best fit parameters of the offset regions.

	OFFSET-1deg				OFFSET-4deg
	Nominal (2 T)	Z_{Ne} free	3 T ($z = 0$)	3 T ($z = 0.048$)	Nominal (2 T)
kT_1 [keV]	$0.111^{+0.009}_{-0.015}$	$0.103^{+0.010}_{-0.008}$	$0.093^{+0.012}_{-0.008}$	$0.093^{+0.012}_{-0.009}$	0.091±0.014
$Norm_1$*	$56.4^{+33.2}_{-11.0}$	$71.2^{+23.8}_{-18.6}$	$82.3^{+24.4}_{-25.5}$	$82.5^{+39.7}_{-25.1}$	$110.8^{+120.1}_{-47.5}$
kT_2 [keV]	$0.250^{+0.028}_{-0.022}$	$0.232^{+0.020}_{-0.012}$	$0.188^{+0.021}_{-0.010}$	$0.185^{+0.027}_{-0.010}$	$0.240^{+0.021}_{-0.015}$
Z_{Ne} ($Z_\odot$)	1.0 (fix)	2.1±0.3	1.0 (fix)	1.0 (fix)	1.0 (fix)
$Norm_2$*	$7.8^{+2.5}_{-2.0}$	$8.6^{+1.4}_{-2.0}$	$15.1^{+6.2}_{-5.2}$	15.8±6.0	15.3±3.0
Γ (fix)	1.4 (fix)	1.4 (fix)	1.4 (fix)	1.4 (fix)	1.4 (fix)
SB†	6.4±0.2	6.4±0.2	6.1±0.2	6.1±0.2	7.5±0.3
kT_3	-	-	$0.861^{+0.068}_{-0.091}$	$0.966^{+0.099}_{-0.088}$	-
Redshift	-	-	0	0.048 (fix)	-
$Norm_3$*	-	-	$1.0^{+0.3}_{-0.2}$	1.5±0.3	-
$\chi^2/d.o.f$	264/136	213/135	199/134	197/134	225/177

* Normalization of the *apec* model divided by a solid angle Ω, assumed in a uniform-sky ARF calculation (20' radius), i.e. $Norm = (1/\Omega)\int n_e n_H dV/(4\pi(1+z)^2 D_A^2)$ cm^{-5} sr^{-1} in unit of 10^{-14}, where D_A is the angular diameter distance.

† Surface brightness of the *power-law* model in the unit of photons s^{-1} cm^{-2} sr^{-1} keV^{-1} at 1 keV.

Table 3. Line centers and surface brightnesses of O VII Kα and O VIII Kα emission.

		ON-FILAMENT	OFFSET-1deg	OFFSET-4deg
O VII Kα	center [keV]	0.569±0.006	$0.572^{+0.001}_{-0.002}$	0.571±0.003
	SB *	$11.8^{+1.6}_{-1.7}$	$12.6^{+0.6}_{-0.7}$	$12.9^{+1.6}_{-1.3}$
O VIII Kα	center [keV]	$0.654^{+0.008}_{-0.006}$	$0.662^{+0.003}_{-0.004}$	$0.651^{+0.005}_{-0.003}$
	SB *	4.3±0.7	$2.8^{+0.2}_{-0.3}$	4.6±0.6

* Surface brightness in the unit of 10^{-7} photons s^{-1} cm^{-2} arcmin^{-2}.

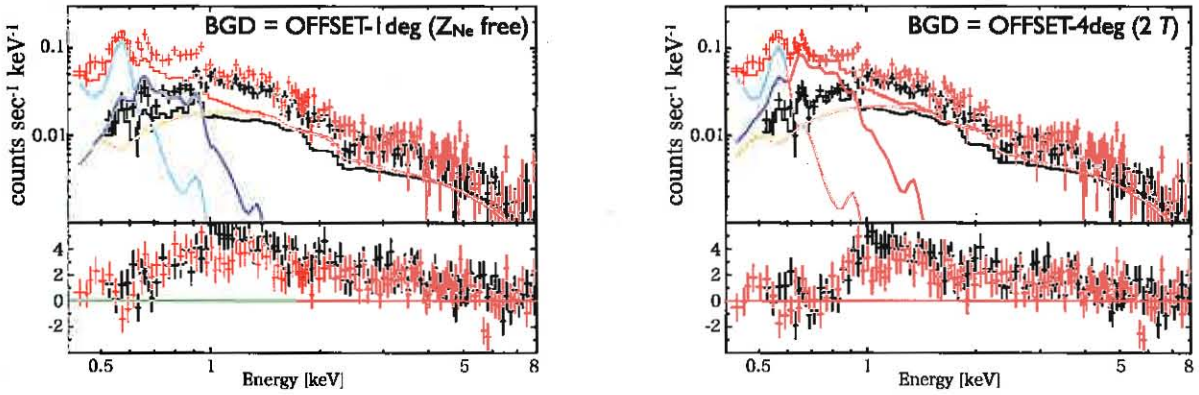

Fig. 5. Spectra in 0.4–8.0 keV in the ON-FILAMENT region. The foreground emission and the CXB are fixed to the best fit parameters obtained in the OFFSET-1deg and the OFFSET-4deg regions, respectively. Left: fitted with the Z_{Ne} free model of the OFFSET-1deg region in Table 2. Right: fitted with the 2 T model of the OFFSET-4deg region in Table 2.

Table 4. Best fit parameters of the ON-FILAMENT region modeling the foreground by fitting with the OFFSET-4deg region simultaneously.

	2 T	3 T		
		$z = 0, Z = 1\ Z_\odot$	$z = 0.048, Z = 1\ Z_\odot$	$z = 0.048, Z = 0.3\ Z_\odot$
f	0.98±0.07	0.90±0.07	0.91±0.07	0.87±0.07
kT_1 [keV]	$0.093^{+0.012}_{-0.006}$	0.091±0.010	0.091±0.010	$0.091^{+0.011}_{-0.008}$
$Norm_1{}^*/f$	$100.9^{+38.3}_{-38.2}$	$110.9^{+68.5}_{-39.2}$	$110.0^{+67.6}_{-39.2}$	$109.0^{+56.9}_{-39.7}$
kT_2 [keV]	$0.250^{+0.019}_{-0.014}$	$0.235^{+0.015}_{-0.012}$	$0.234^{+0.015}_{-0.012}$	$0.235^{+0.016}_{-0.012}$
$Norm_2{}^*/f$	14.3±2.4	16.0±2.5	16.0±2.5	15.9±2.5
Γ (fix)	1.4 (fix)	1.4 (fix)	1.4 (fix)	1.4 (fix)
$SB^\dagger$	13.3±0.3	12.0±0.5	11.7±0.6	$10.0^{+1.4}_{-1.7}$
kT_3		$1.3^{+0.3}_{-0.2}$	$1.6^{+0.6}_{-0.3}$	$2.0^{+0.8}_{-0.5}$
Redshift		0	0.048 (fix)	0.048 (fix)
$Z\ (Z_\odot)$		1.0 (fix)	1.0 (fix)	0.3 (fix)
$Norm_3{}^*$		3.6±1.0	$6.6^{+5.3}_{-3.1}$	$22.7^{+8.4}_{-8.3}$
$\chi^2/d.o.f$	568/398	497/396	496/396	481/396

* Normalization of the *apec* models. See notes in Table 2 for the definition of the normalization. The foreground emission is determined by fitting with the OFFSET-4deg region simultaneously and their normalizations are rescaled by the factor of f.

† Surface brightness of the *power-law* model in the unit of photons s^{-1} cm^{-2} keV^{-1} sr^{-1} at 1 keV.

Table 5. Best fit parameters of the ON-FILAMENT region modeling the foreground by fitting with the OFFSET-1deg region simultaneously.

	2 T	3 T		
		$z = 0, Z = 1\ Z_\odot$	$z = 0.048, Z = 1\ Z_\odot$	$z = 0.048, Z = 0.3\ Z_\odot$
f	1.24±0.08	1.18±0.08	1.16±0.08	1.10±0.08
kT_1 [keV]	$0.101^{+0.011}_{-0.007}$	$0.100^{+0.010}_{-0.006}$	$0.100^{+0.010}_{-0.006}$	$0.100^{+0.010}_{-0.006}$
$Norm_1{}^*/f$	$72.2^{+21.5}_{-20.8}$	$74.5^{+21.7}_{-20.4}$	$75.3^{+21.8}_{-20.8}$	$74.6^{+21.9}_{-20.3}$
kT_2 [keV]	$0.238^{+0.014}_{-0.011}$	$0.231^{+0.013}_{-0.010}$	$0.229^{+0.012}_{-0.010}$	$0.229^{+0.012}_{-0.010}$
$Z_{Ne}\ (Z_\odot)$	$2.2^{+0.3}_{-0.2}$	$2.1^{+0.3}_{-0.2}$	2.1±0.3	2.1±0.3
$Norm_2{}^*/f$	$8.8^{+1.3}_{-1.7}$	9.4±1.3	9.6±1.3	9.5±1.3
Γ (fix)	1.4 (fix)	1.4 (fix)	1.4 (fix)	
$SB^\dagger$	13.5±0.4	$11.0^{+1.3}_{-1.5}$	$10.9^{+0.9}_{-1.3}$	$9.1^{+1.4}_{-1.9}$
kT_3		$2.1^{+0.9}_{-1.2}$	$2.1^{+0.8}_{-0.5}$	$2.3^{+0.9}_{-0.6}$
Redshift		0	0.048 (fix)	0.048 (fix)
$Z\ (Z_\odot)$		1.0 (fix)	1.0 (fix)	0.3 (fix)
$Norm_3{}^*$		$9.2^{+6.2}_{-6.8}$	$11.1^{+5.9}_{-4.8}$	$27.5^{+8.5}_{-7.7}$
$\chi^2/d.o.f$	570/356	499/354	497/354	475/354

* Normalization of the *apec* models. See notes in Table 2 for the definition of the normalization. The foreground emission is determined by fitting with the OFFSET-1deg region (Z_{Ne} free model in Table 2) simultaneously and their normalizations are rescaled by the factor of f.

† Surface brightness of the *power-law* model in the unit of photons s^{-1} cm^{-2} keV^{-1} sr^{-1} at 1 keV.

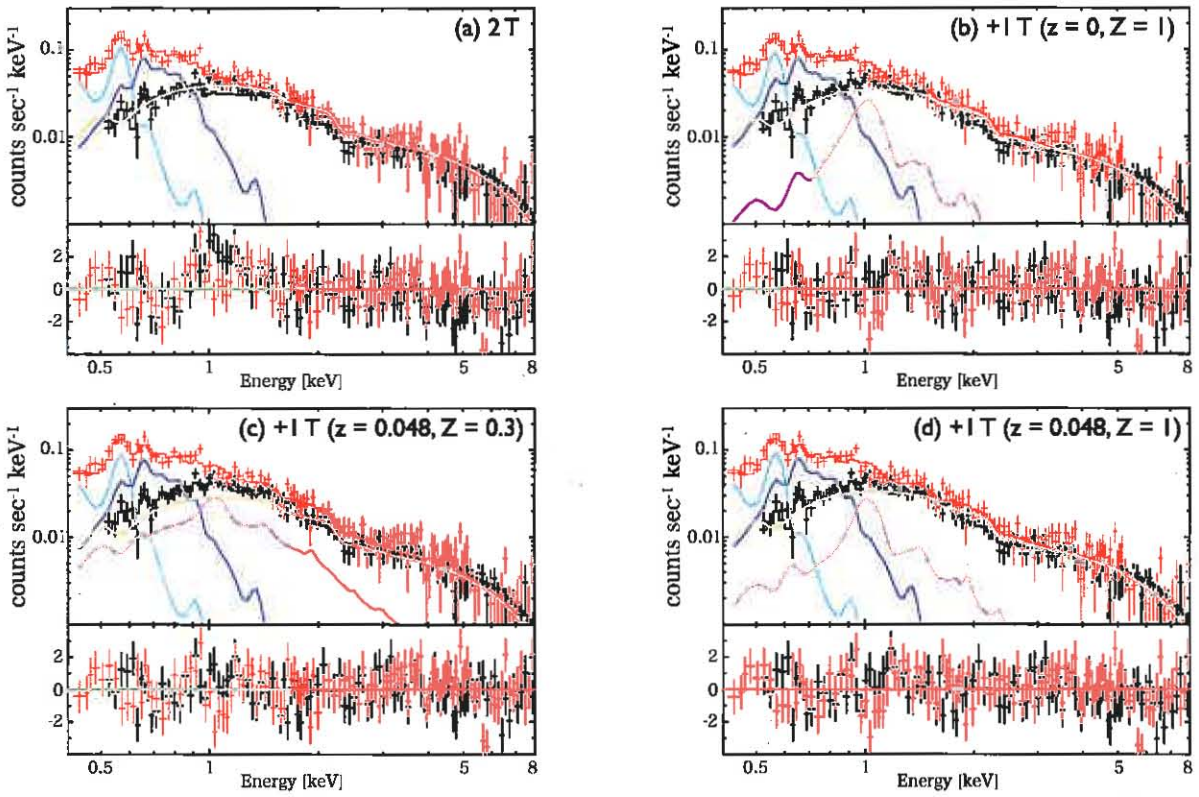

Fig. 6. Spectra in 0.4–8.0 keV in the ON-FILAMENT region. The foreground emission is determined by fitting with the OFFSET-4deg region (2 *T* in Table 2) simultaneously and spectra of the OFFSET-4deg are removed in this figure. Red and black data are for BI and FI sensors, respectively. The spectral data are the same for the four panels, but the fitted models and residuals are different. Top left: fitted with typical foreground/background model, i.e., the sum of (1), (2) and (3) of Fig. 3. Top right: fitted with a model with a sum of (1), (2), (3), and another thin thermal plasma. The redshift and abundance are $z = 0$ and $Z = 1$ solar, respectively. Bottom left: same as top right, but $z = 0.048$ and $Z = 0.3$ solar. Bottom right: same as top right, but $z = 0.048$ and $Z = 1$ solar. Cyan, blue, orange and magenta lines indicate LHB+SWCX, MWH, CXB, and the additional higher temperature plasma, respectively. The photon index of the CXB is fixed to be 1.4.

We also evaluated line centers and the surface brightness of O VII Kα and O VIII Kα emission lines in the similar manner as we did for offset regions. The best-fit values are shown in Table 3. The center energies in the ON-FILAMENT region are again consistent with zero redshift within the statistical error and the typical energy determination accuracy of the *Suzaku* XIS.

3.3. *Upper limit of intensities and densities of the redshifted component*

We evaluated the 2σ upper limit of WHIM density at $kT = 0.2 - 0.3$ keV, using upper limits of redshfited O VII Kα and O VIII Kα emission line intensities, with the same method as Takei et al. (2007b). To determine the upper limits, we added in the model described in § 3 two Gaussian functions that represent redshifted O VII Kα and O VIII Kα emission lines, i.e., we used the following models: *apec*$_1$ + *phabs*× (*vapec*$_2$+ *power-law*) for the OFFSET-1deg region, and *apec*$_1$ + *phabs*× (*apec*$_2$+ *apec*$_3$+ *power-law*) for the ON-FILAMENT region. Temperature of the *apec* models was fixed to the best fit values and the energy of the O lines were set to be the redshifted values (0.544 keV for O VII Kα and 0.624 keV for O VIII Kα). We assume the velocity dispersion of the line is negligible and the widths of the Gaussian were set to 0. The upper limits of O VII Kα and O VIII Kα lines for the OFFSET-1deg region are, respectively, 4.2×10^{-7} and 4.0×10^{-8} photons s^{-1} cm^{-2} arcmin^{-2}. For the ON-FILAMENT region, they are 2.4 and 1.3×10^{-7} photons s^{-1} cm^{-2} arcmin^{-2} with the OFFSET-1deg background template and 9.0 and 1.5×10^{-7} photons s^{-1} cm^{-2} arcmin^{-2} with the OFFSET-4deg template.

As described in Takei et al. (2007b), we constrain the density of the WHIM assuming a uniform density and temperature distribution, as a function of the temperature. We adopted 3×10^6 K which gave the maximum emissivity of O VIII Kα line.

The 2σ upper limit intensity of O VIII Kα in the ON-FILAMENT region with the OFFSET-4deg background template, $I < 1.5 \times 10^{-7}$ photons s^{-1} cm^{-2} arcmin^{-2}, gives a constraint on the gas density. We assumed the line-of-sight length $L = 3$ Mpc, which is about the same as the distance between A3556 and A3558. The density is estimated as

$$n_H < 7.7 \times 10^{-5} \text{ cm}^{-3} \left(\frac{Z}{0.1\ Z_\odot}\right)^{-1/2} \left(\frac{L}{3 \text{ Mpc}}\right)^{-1/2}. \quad (1)$$

Here an electron-to-hydrogen number density ratio n_e/n_H of 1.2 is assumed because H and He are fully ionized. The overdensity $\delta \equiv n_H/\bar{n}_H - 1$ is calculated to be

$$\delta < 380 \left(\frac{Z}{0.1\ Z_\odot}\right)^{-1/2} \left(\frac{L}{3 \text{ Mpc}}\right)^{-1/2} \quad (2)$$

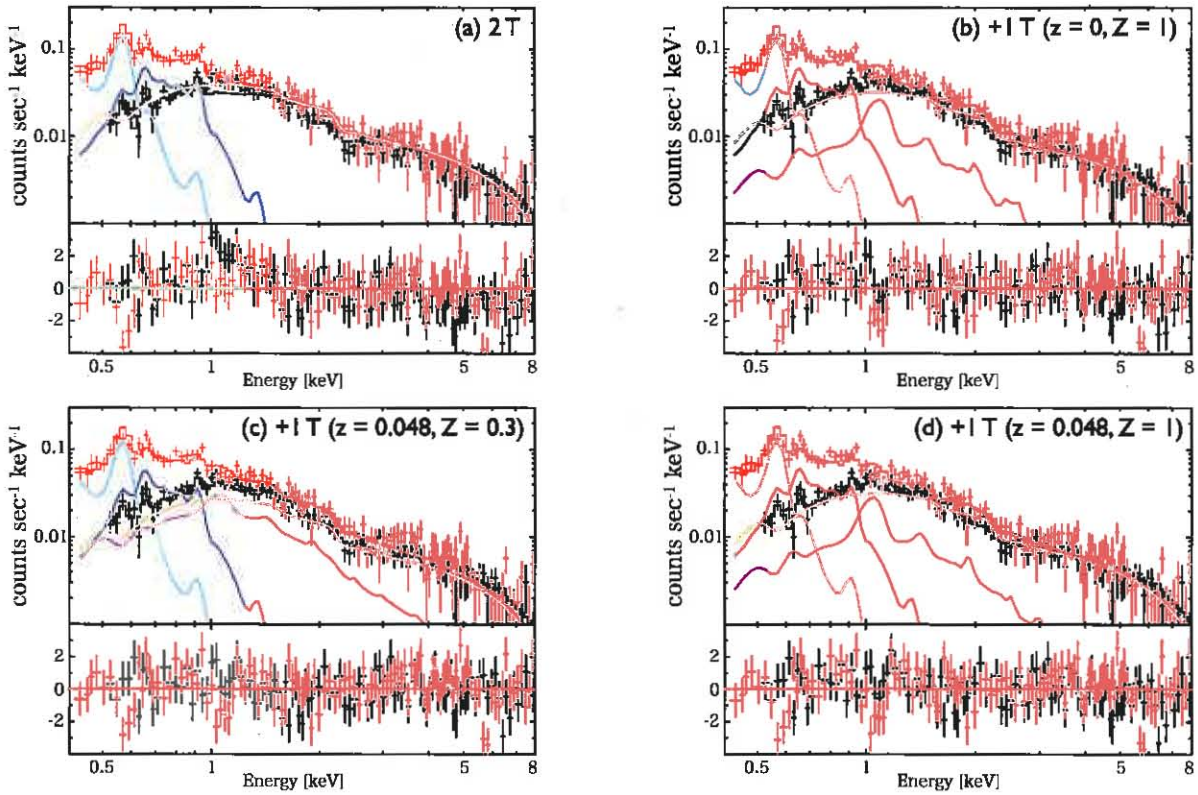

Fig. 7. The same as Figure 6, but the Z_{Ne} free model of OFFSET-1deg region in Table 2 is uesd as the foreground emission.

We can also constrain the density of the redshifted thermal plasma, i.e., the supercluster plasma, from the emission measure of the continuum emission as discussed in § 4.1. To extract the upper limit of the density of the supercluster plasma, we assumed all of the observed excess emission to be due to the supercluster plasma. From the definition of the *norm* in the *apec* model,

$$n_H < 1.1 \times 10^{-5} (norm)^{1/2} \left(\frac{L}{3\ \mathrm{Mpc}} \right)^{-1/2} . \quad (3)$$

With *norm* = 1.8, we obtained 1.5×10^{-5} $(L/3\ \mathrm{Mpc})^{-1/2}$ cm^{-3} and $\delta < 70$ $(L/3\ \mathrm{Mpc})^{-1/2}$ for the OFFSET-1deg region. For the ON-FILAMENT region with the OFFSET-1deg background template, *norm* = 37.9 indicated 6.8×10^{-5} $(L/3\ \mathrm{Mpc})^{-1/2}$ cm^{-3} and $\delta < 330$ $(L/3\ \mathrm{Mpc})^{-1/2}$. The corresponding continuum flux F in the ON-FILMENT region in 0.5–2.0 keV is $F = 1.3^{+0.4}_{-0.3} \times 10^{-15}$ ergs s^{-1} cm^{-2} arcmin^{-2} with the OFFSET-1deg background template. The obtained flux is consistent with that with the OFFSET-4deg background template. Resultant 2σ upper limits of n_H and δ are summarized in Table 6. In the case of O VII Kα, we assumed 2×10^6 K corresponding to the maximum emissivity of O VII Kα lines.

4. Discussion

4.1. *Origin of the redshifted thermal emission*

As reported in § 1, excess emission compared to the surrounding background level was detected with *ROSAT* (Kull & Böhringer 1999) in 0.1–2.4 keV. The location was between A3558 and A3556, namely the same region as in the present Suzaku study. The intensity of this excess emission in 0.1–2.4 keV is 2×10^{-15} ergs s^{-1} cm^{-2} arcmin^{-2}. The intensities of the additional redshifted thermal component in the *Suzaku* spectrum are $1.9^{+0.6}_{-0.5} \times 10^{-15}$ ergs s^{-1} cm^{-2} arcmin^{-2} and $1.6^{+0.6}_{-0.5} \times 10^{-15}$ ergs s^{-1} cm^{-2} arcmin^{-2} with the OFFSET-1deg and the OFFSET-4deg background templates, respectively. This is consistent with the reported excess with *ROSAT* within the statistical error.

The possible origins of this excess emission are (1) cluster emission at the outskirt region, (2) stray light from the inner bright cluster emission, (3) unresolved point sources and (4) plasma associated with the supercluster. First, we focused on the first two possibilities. According to Bardelli et al. 1996, surface brightness distribution of bright cluster A3558 within < 0.55 (R_{vir}) shows a roughly elliptical shape with a superposition of 3 components: the A3558 cluster emission (an elliptical King model with $\beta = 0.61$), the central galaxy emission (approximated by a gaussian) and the spatially constant background. This β value is about 20% higher than that of ASCA result by Fukazawa et al. 2004 obtained by fitting with a spherically symmetric β model. Therefore, if observed excess emission by *Suzaku* is associated with A3558, the intensity along the radial direction from A3558 should monotonously decrease in accordance with the β model profile. Thus, we examined the unabsorbed intensity profile along the radial direction of A3558 with 4 annular regions which are 0.54 to 0.74, 0.74 to 0.92, 0.92 to 1.1, and 1.1 to 1.24 R_{vir}, respectively. The extracted regions and the intensities are shown in Figure 8. In

Table 6. 2σ upper limit densities and overdensities using the redshifted O VII Kα, O VIII Kα and, continuum emissions.

REGION		ON-FILAMENT		OFFSET-1deg
O VII ($T = 2\times10^6$ K, $Z = 0.1\ Z_\odot$ and, $L = 3$ Mpc)		BGD=OFFSET-1deg*	BGD=OFFSET-4deg†	
SB	10^{-7} photons s^{-1} cm^{-2} arcmin^{-2}	2.4	9.0	4.2
n_H	10^{-5} cm^{-3}	7.9	15	10
δ		390	750	510
O VIII ($T = 3\times10^6$ K, $Z = 0.1\ Z_\odot$ and, $L = 3$ Mpc)				
SB	10^{-7} photons s^{-1} cm^{-2} arcmin^{-2}	1.3	1.5	0.4
n_H	10^{-5} cm^{-3}	7.3	7.7	4.0
δ		360	380	200
Continuum ($L = 3$ Mpc)				
$n_H^\ddagger$	10^{-5} cm^{-3}	6.8	6.4	1.5
$\delta^\ddagger$		330	310	70

* The ($Z_{\rm Ne}$ free) column in Table 2.

† The Nominal column in Table 2 right.

‡ Extracted by the *Norm* value in the *apec* model of the redshifted thermal plasma of the ($z = 0.048$, $Z = 0.3\ Z_\odot$) column in Table 4 and 5 right.

this analysis, we fixed the X-ray background emission using the best-fit parameters shown in Table 4 and 5 (right) which was evaluated from the data in the entire FOV. We confirmed that resultant intensities were consistent with each other between the OFFSET-1deg and the OFFSET-4deg background templates in each region. Figure 8 (right) shows the intensity using the OFFSET-1deg background template and that the intensity decrease from the first to the second bins.

For comparison, we plotted in Figure 8 the surface brightness of A3558 in Bardelli et al. 1996 extrapolated from the inner region data within $\sim 0.55R_{\rm vir}$ (red solid curve). Bump-like structures in this profile are caused by the ellipticity of A3558. Clearly, the simple extrapolated intensity gives significantly brighter emission than the observed data. This is possibly caused by a decrease of temperature and/or density in the outer region. We modified the β value from the best-fit value 0.61 in Bardelli et al. 1996 to 0.65 and 0.70 whereby conserving the total luminosity within $0.55R_{\rm vir}$ to be consistent with the data. These brightness curves are also indicated in Figure 8. Thus if the observed excess emission is originated from the outer region of A3558, either the slope should become steeper or the intensity should drop by a factor of ~ 3 below the simple extrapolated level.

The rightmost bin in Figure 8, which is the farthest from A3558, shows an intensity rise and requires some additional component. Therefore, we estimated the influence from another nearby cluster A3556, in which its surface brightness was derived from the index of optical galaxy distribution whose b_j magnitude was less than 18 reported in Bardelli et al. 1998 and the X-ray luminosity by Akimoto et al. (2003). We assumed that the X-ray brightness is approximated by a β model and tried 3 β values of 0.5, 0.6 and 0.7 by conserving the total luminosity to be the same. Fukazawa et al. 2004 reported the β value of A3556 to be much smaller ($0.19^{+0.06}_{-0.02}$) than our assumption. This result may be caused by the faintness of this cluster. Thus in this analysis, we assumed typical β values. These β-model profiles are shown in Figure 8 (right) by magenta, cyan and orange curves for $\beta = 0.5$, 0.6 and 0.7, respectively. Observed excess emission can be expressed by a superposition of the emission from the nearby clusters A3556 and A3558. However, to explain the observed data, the slope of A3558 required in the outer region needed to be steeper than that in the inner region or the cluster emission fell down more rapidly by a factor of ~ 3 at the outer region. Again this may be caused by a decrease of either temperature or density in the outer region.

Next, we evaluated the possible contamination from the inner bright emission of A3558 using *xissim* ftool in each bin. As the emission model, the thin thermal plasma model *apec* was employed with the parameters set to be the best-fit values obtained by ASCA (Akimoto et al. 2003, $kT = 5.6$ keV, $Z = 0.34Z_\odot$) within 12′ from the center of A3558. Spatial distribution of photons was weighted by the assumed surface brightness (β-model distribution for A3556 and an elliptical β-model distribution for A3558 as described above), and the number of photons was equivalent to 10 Ms exposure to keep the statistical error small. We examined the original position of all the simulated photons and extracted the ratio of photon counts originated from the inner cluster region to the total detected ones in the energy range 0.5 to 2.0 keV. As a result, the contribution from the inner region is < 30% (less than 10% in most of the regions in the FOV) in the observed region.

Thirdly, we focused on the influence of unresolved point sources. According to Bardelli et al. 1996, 22 other X-ray sources around the A3558 cluster were detected and their detection limit was 2.9×10^{-14} ergs s^{-1} cm^{-2} in 0.5-2.0 keV.

Among them, only 1 source with $F_X = 6.4 \times 10^{-14}$ ergs s^{-1} cm^{-2} was in the FOV of *Suzau* ON-FILAMENT region. This source was already excluded in our analysis. In Bardelli et al. 1998, the galaxy density of A3556 and A3558 is about 0.01 and 0.05 arcmin^{-2} respectively in our observed region and thus the expected total number of galaxies in the *Suzaku* FOV is about 10. Therefore, if each galaxy has the flux of the detection limit of 2.9×10^{-14} ergs s^{-1} cm^{-2} in 0.5-2.0 keV, the total flux as the sum of these galaxies can not reach the observed flux of $\sim 3.5 \times 10^{-13}$ ergs s^{-1} cm^{-2}. As for the forth possibility of the plasma associated with the supercluster, although the observed excess can be expressed by a superimposed emission from A3556 and A3558, this possibility is not excluded.

As shown above, the observed excess emission can be expressed either by the superposition of emission from nearby clusters A3556 and A3558 or by the supercluster plasma. Since the supercluster space would not be virialized yet, the observed temperature of the excess emission, $2.3^{+0.9}_{-0.6}$ or $2.0^{+0.8}_{-0.5}$ keV in the case the OFFSET-1deg and the OFFSET-4deg background templates, is probably too high for the supercluster plasma. On the other hand, this temperature is about 40% of the level measured in the central 12 arcmin region of A3558 (Akimoto et al. 2003). This ratio is consistent with the other recent results for cluster outskirts around the virial radius (George et al. 2009; Kawaharada et al. 2010; Hoshino et al. 2010; Simionescu et al. 2011). If this excess is caused by the superposition of two nearby clusters A3556 and A3558, we expect no temperature jump in the observed region. This is consistent with the ON-FILAMENT results.

4.2. *Constraint on the WHIM*

Redshifted O emission lines from the WHIM have been searched for with *Suzaku* in several clusters of galaxies and superclusters. Although the sensitivity of *Suzaku* is better than previous missions, no positive detection has been obtained. Figure 9 summarizes the upper limits of O VII and O VIII surface brightness obtained with *Suzaku*. The data for Shapley is from ON-FILAMENT observation of this work, and the others are from literature (Takei et al. 2007b; Takei et al. 2007a; Sato et al. 2010; Hoshino et al. 2010; Fujita et al. 2008; Akamatsu et al. 2011). The sensitivity depends on observation dates due to degradation and uncertainty of effective area in the low energy band. It also depends on the redshift of objects, because Galactic strong O VII line may overlap with the redshifted O VIII line for some redshift range. The latter is the reason of relatively high upper limits of the O VII line in the Shapley supercluster. If we exclude this unfortunate case, the upper limits in general reach $\sim 10^{-7}$ photons cm^{-2} s^{-1} arcmin^{-2} for both O VII and O VIII lines. The fact that redshifted O lines have not so far been significantly detected indicates that the average temperature and density of the WHIM associated with clusters of galaxies or superclusters lie outside of the detectable range.

In the calculation of the upper limit of δ shown in § 3.3, we assumed a fixed temperature of $T = 3 \times 10^6$ K. The left panel of Figure 10 shows our calculation showing the temperature dependence under the assumption of CIE, based on the SPEX code (Kaastra et al. 1996). The plot shows $\delta\ (I_{-7})^{-1/2}\ (L/3\ \mathrm{Mpc})^{1/2}\ (Z/0.1Z_\odot)^{1/2}$ as a function of temperature, where $I_{-7} = I/10^{-7}$ photons cm^{-2} s^{-1} arcmin^{-2}. Since δ is proportional to $I^{1/2}\ L^{-1/2}\ Z^{-1/2}$ for a fixed temperature, the curves in the plot correspond to the upper limit of δ assuming $I_{-7} = 1$, $L = 3$ Mpc, and $Z = 0.1\ Z_\odot$. The solid line indicates the upper limit determined by the O VII line, while the dashed line is by the O VIII line. When both the O VII and O VIII lines give the same upper limits, the O VII constraint is tighter in the temperature range $T < 3 \times 10^6$ K, while O VIII is more sensitive in the higher temperatures. The *Suzaku* detectability ($I_{-7} \lesssim 1$ for both O VII and O VIII) corresponds to $\delta < 400$ in a relatively wide temperature range: $1.4 \times 10^6\ \mathrm{K} < T < 5 \times 10^6$ K.

In the higher temperature range where the O lines are not sensitive (i.e., $T > 5 \times 10^6$ K), we expect continuum emission to give a better constraint. The right panel of Figure 10 shows $\delta\ (F_{-15})^{-1/2}\ (L/3\ \mathrm{Mpc})^{1/2}$ as a function of temperature, where $F_{-15} = F/10^{-15}$ ergs cm^{-2} s^{-1} arcmin^{-2} and F is the flux in 0.5–2.0 keV. Solid and dashed lines are for $Z = 0.1\ Z_\odot$ and $Z = 0.3\ Z_\odot$, respectively.

The flux of the continuum observed in the ON-FILAMENT region is $F_{-15} = 1.0 \pm 0.2$. Hence, the continuum from $\delta \lesssim 400$ and $T \gtrsim 5 \times 10^6$ K plasma can lie statistically above the detection limit of *Suzaku*. However, as discussed in § 4.1, the origin of such a weak continuum is hard to be identified, because of the uncertainty in the Galactic emission and of the difficulty in spectroscopically constraining the redshift with the CCD energy resolution. Although the detection limit considering the systematics is not clear, there have been no strong indications of $T < 10^7$ K continuum associated with clusters or superclusters from *Suzaku* observations.

To summarize the search for the WHIM signal with *Suzaku*, we can exclude the temperature-density region with $1.4 \times 10^6\ \mathrm{K} < T < 5 \times 10^6$ K and average $\delta > 400$ or with $T < 10^7$ K and average $\delta \gg 400$. Such WHIM gas is not typically associated with clusters of galaxies and superclusters.

Werner et al. (2008) detected continuum emission in a bridge structure between A222 and A223. The spectrum can be represented by a CIE plasma with $kT = 0.9$ keV and $\delta = 150$, assuming $L = 15$ Mpc. Because of the very large line-of-sight depth, the density is lower than the detection limit shown in Figure 10 and the temperature is higher than the level effectively probed with O emission lines. This result also suggests that the overdensity of the intergalactic plasma, especially with $T \sim (2\text{–}3) \times 10^6$ K, is less than 400, which is consistent with our *Suzaku* observations.

There are several other claims from CCD observations of possible detection of WHIM signals including O lines (e.g., Kaastra et al. 2003; Finoguenov et al. 2003). The reported intensities of O lines are stronger than the upper limit from *Suzaku*. The reason of this discrepancy is thought to be the overestimation of intergalactic emission in those reports, due to insufficient modeling of the detector response and background, or due to spatial and temporal variation of foreground emission (e.g., Bregman & Lloyd-Davies 2006; Takei et al. 2008). Hence, the true signals from the WHIM are likely to be lower than the upper limits obtained with *Suzaku*.

The observational constraint on δ can be compared with predictions from cosmological numerical simulations. Recently many extensive simulation studies have been performed by several groups with various physical processes considered as controlling parameters (e.g., Bertone et al. 2010; Schaye et al.

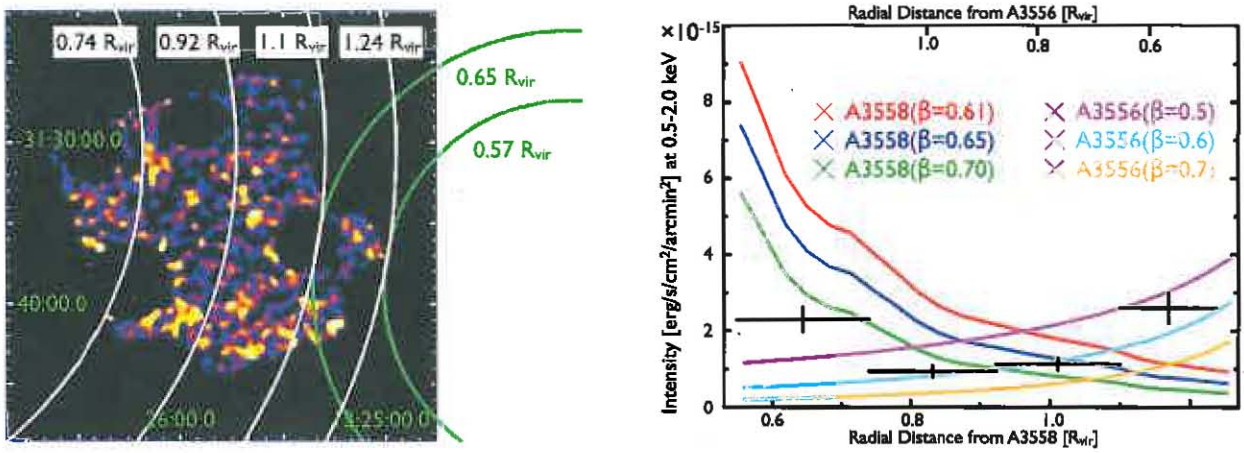

Fig. 8. Left: Regions for the spectral analysis are shown on the XIS BI image with radial distances from A3558 (white) and A3556 (green). Right: Radial profile of the observed excess emission compared with the expected ones. Black symbols show the observed excess. Curves falling to the right are expected profiles of A3558 assuming $\beta = 0.61$ (red), 0.65 (blue) and 0.70 (green), respectively. Other curves show brightness profiles of A3556 assuming $\beta = 0.5$ (magenta), 0.6 (cyan) and 0.7 (orange), respectively.

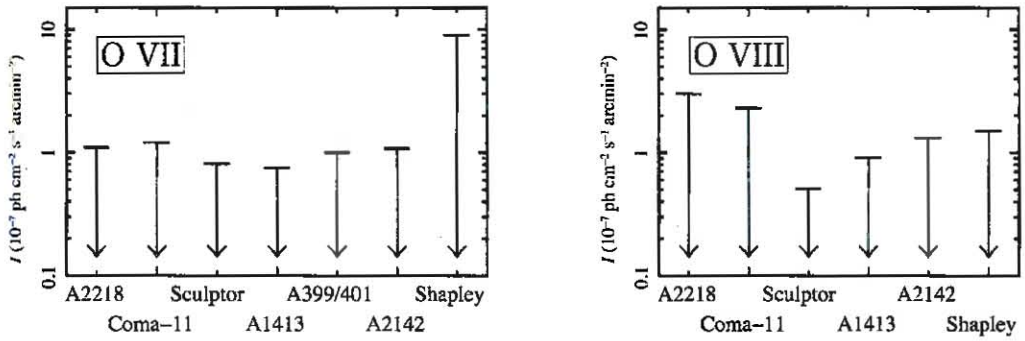

Fig. 9. Upper limits of redshifted Oxygen emission lines from *Suzaku* observations. Left: O VII; right: O VIII. References are: A2218 (Takei et al. 2007b), Coma-11 (Takei et al. 2007a), Sculptor (Sato et al. 2010), A1413 (Hoshino et al. 2010), A399/401 (Fujita et al. 2008) and A2142 (Akamatsu et al. 2011). Shapley data are from this work.

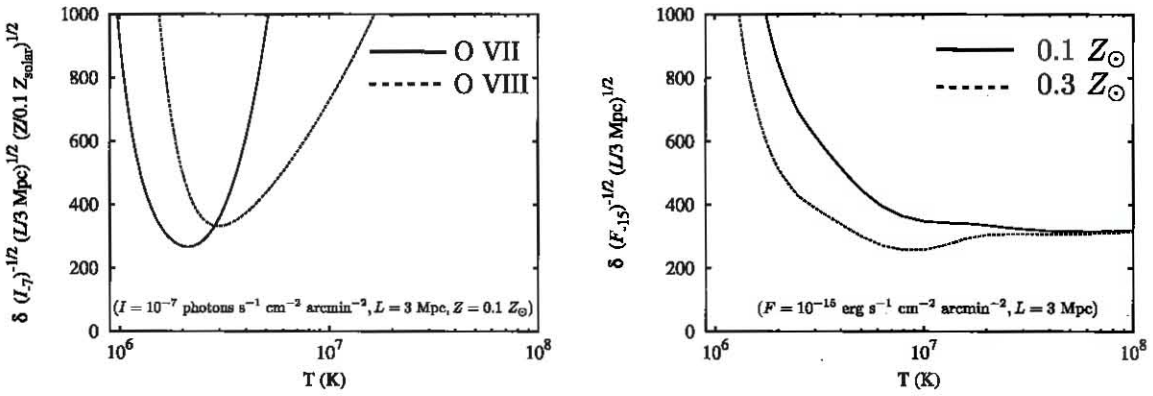

Fig. 10. The upper limit of overdensity (δ) as a function of temperature. Left: the upper limit from O VII (solid) and O VIII (dashed) emission lines. $I = 10^{-7}$ photons s^{-1} cm^{-2} arcmin^{-2} ($I_{-7} = 1$), $L = 3$ Mpc and $Z = 0.1$ $Z_\odot$ are assumed. Right: the upper limit from continuum emission. $F = 10^{-15}$ ergs s^{-1} cm^{-2} arcmin^{-2} = 1 ($F_{-15} = 1$) and $L = 3$ Mpc are assumed. Solid and dashed lines are with $Z = 0.1$ $Z_\odot$ and $Z = 0.3$ $Z_\odot$, respectively.

2010; Wiersma et al. 2010; Tornatore et al. 2010; Ursino et al. 2010; Wiersma et al. 2011). Although the phase diagram of the WHIM depends on the details of physical processes such as galactic wind, AGN feedback, metal line cooling, photoionization by background radiation, and sub-resolution turbulence, the simulations in general predict the high-density end of the WHIM to have $\delta > 400$ and $T > 10^6$ K. However, the simulations also predict that such high density regions are typically smaller than the integrated volume with current *Suzaku* observations. This is qualitatively seen by comparing Figure 6 of Branchini et al. (2009) and Figure 4 (top left) of Takei et al. (2011). Both plots show the phase diagram of the WHIM from the same simulation, but the latter shows average quantities in a 500 kpc × 500 kpc × 3 Mpc volume, which is similar to the integrated volume in this work (~ 1 Mpc × 1 Mpc × 3 Mpc). Aa a result of the averaging, no WHIM can be identified to have $\delta > 400$ and $T < 10^7$ K. We should emphasize that the plot is just the result from one particular simulation, and different simulation parameters (i.e., different assumption of the physical processes) may lead to different results. Nevertheless, we expect this conclusion to hold for a wide range of input parameters, at least in a qualitative manner. Simulation in Ursino & Galeazzi (2006) also indicates that the continuum emission from the WHIM, after integrating $> 10' \times 10'$ FOV, is smaller than 20 photons s^{-1} cm^{-2} sr^{-1} (0.375–0.950 keV), which is consistent with this work.

The discussion indicates that the clear detection of the WHIM X-ray signals is challenging with CCD cameras. Spatially resolved spectroscopy for $L \gtrsim 10$ Mpc path length may work as shown in Werner et al. (2008), but this requires a fortunate orientation of the cosmological filamentary structure. Otherwise, the sensitivity on the surface brightness needs to be improved by ~one order of magnitude, considering $I \propto \delta^2$. This will be achieved by future missions equipped with a microcalorimeter array, which enables us to pick up weak redshifted O lines by an excellent energy resolution of ΔE = a few eV. Dedicated X-ray missions have been proposed with instruments with a few eV energy resolution and ~deg^2 FOV, such as *DIOS*, *EDGE*, *XENIA* and *ORIGIN* (Ohashi et al. 2010; Piro et al. 2009; Burrows et al. 2010; den Herder et al. 2011). Even though these missions are not formally approved for future space program, we stress that such wide-field missions are capable of not only detecting the WHIM but also studying its 3D structure by mapping the redshifted O emission lines (Takei et al. 2011).

5. Conclusions

We examined the X-ray spectral properties of inter-cluster regions in the Shapley supercluster based on three *Suzaku* observations named as the OFFSET-4deg, OFFSET-1deg and ON-FILAMENT regions. Although redshifted Oxygen emission lines were not detected, the OFFSET-1deg and the ON-FILAMENT regions indicated excess continuum emission compared with the OFFSET-4deg region whose spectrum could be fitted with the typical model for blank skies. These additional emissions were represented by thermal models with $kT \sim 1$ keV and ~ 2 keV in the OFFSET-1deg and the ON-FILAMENT regions, respectively. For the origin of the 1 keV emission, Galactic (Ne-rich or high temperature) and supercluster plasma were both statistically acceptable. The 2 keV plasma between A3556 and A3558 is likely to be the ICM or supercluster origin considering the radial intensity profile. However, the obtained temperature of $2.3^{+0.9}_{-0.6}$ and $2.0^{+0.8}_{-0.5}$ keV is too high for a supercluster plasma and the observed drop of temperature is consistent with the *Suzaku* measurements of other clusters. Assuming this plasma to be the WHIM bound in the region between A3556 and A3558, we derived an upper limit for the redshifted O VIII intensity to be 1.5×10^{-7} photons s^{-1} cm^{-2} $arcmin^{-2}$. This corresponds to an overdensity of $\sim 380(Z/0.1\ Z_\odot)^{-1/2}\ (L/3\ \mathrm{Mpc})^{-1/2}$, assuming $T = 3 \times 10^6$K.

Finally, we summarized the previous *Suzaku* observations on the WHIM search including this work and discussed the feasibility about the constraint on the overdensity of the WHIM using *Suzaku* XIS. Consequently, an overdensity of < 400 can be detectable using O VII and O VIII emission lines for a temperature range 1.4×10^6 K $< T < 5 \times 10^6$ K and a continuum emission fof $T > 5 \times 10^6$ K. Considering the *Suzaku* results so far obtained, an interpretation that typical line-of-sight integrated average overdensity is < 400 can be derived.

Acknowledgement

I. M. is grateful to Kentaro Someya, Hiroshi Yoshitake, Kazuhiro Sakai and Prof. Kazuhisa Mitsuda for useful advice and discussion. Part of this work was financially supported by the Ministry of Education, Culture, Sports, Science and Technology, Grant-in Aid for Scientific Research 10J07487, 15340088, 20340041, 21224003 and 22111513.

References

Akamatsu, H., Hoshino, A., Ishisaki, Y., Ohashi, T., Sato, K., Takei, Y., & Ota, N. 2011, ArXiv e-prints, 1106.5653
Akimoto, F., Kondou, K., Furuzawa, A., Tawara, Y., & Yamashita, K. 2003, ApJ, 596, 170
Bardelli, S., Zucca, E., Malizia, A., Zamorani, G., Scaramella, R., & Vettolani, G. 1996, A&A, 305, 435
Bardelli, S., Zucca, E., Zamorani, G., Vettolani, G., & Scaramella, R. 1998, MNRAS, 296, 599
Bautz, M. W., et al. 2009, PASJ, 61, 1117
Bertone, S., Schaye, J., Dalla Vecchia, C., Booth, C. M., Theuns, T., & Wiersma, R. P. C. 2010, MNRAS, 407, 544
Branchini, E., et al. 2009, ApJ, 697, 328
Bregman, J. N., & Lloyd-Davies, E. J. 2006, ApJ, 644, 167
Buote, D. A., Zappacosta, L., Fang, T., Humphrey, P. J., Gastaldello, F., & Tagliaferri, G. 2009, ApJ, 695, 1351
Burrows, D. N., Hartmann, D., Kouveliotou, C., Piro, L., den Herder, J., & Ohashi, T. 2010, in Society of Photo-Optical Instrumentation Engineers (SPIE) Conference Series, Vol. 7732, Society of Photo-Optical Instrumentation Engineers (SPIE) Conference Series
Cen, R., & Ostriker, J. P. 1999, ApJ, 514, 1
Danforth, C. W. 2009, in American Institute of Physics Conference Series, Vol. 1135, American Institute of Physics Conference Series, ed. M. E. van Steenberg, G. Sonneborn, H. W. Moos, & W. P. Blair , 8–15
Danforth, C. W., & Shull, J. M. 2005, ApJ, 624, 555
—. 2008, ApJ, 679, 194
Danforth, C. W., Stocke, J. T., & Shull, J. M. 2010, ApJ, 710, 613
Davé, R., et al. 2001, ApJ, 552, 473

den Herder, J.-W., et al. 2011, Experimental Astronomy, 30
Dickey, J. M., & Lockman, F. J. 1990, ARA&A, 28, 215
Ezoe, Y., Ebisawa, K., Yamasaki, N. Y., Mitsuda, K., Yoshitake, H., Terada, N., Miyoshi, Y., & Fujimoto, R. 2010, PASJ, 62, 981
Fabian, A. C. 1991, MNRAS, 253, 29P
Fang, T., Buote, D. A., Humphrey, P. J., Canizares, C. R., Zappacosta, L., Maiolino, R., Tagliaferri, G., & Gastaldello, F. 2010, ApJ, 714, 1715
Finoguenov, A., Briel, U. G., & Henry, J. P. 2003, A&A, 410, 777
Fujimoto, R., et al. 2004, PASJ, 56, L29
—. 2007, PASJ, 59, 133
Fujita, Y., Tawa, N., Hayashida, K., Takizawa, M., Matsumoto, H., Okabe, N., & Reiprich, T. H. 2008, PASJ, 60, 343
Fukazawa, Y., Makishima, K., & Ohashi, T. 2004, PASJ, 56, 965
Galeazzi, M., Gupta, A., & Ursino, E. 2009, ApJ, 695, 1127
George, M. R., Fabian, A. C., Sanders, J. S., Young, A. J., & Russell, H. R. 2009, MNRAS, 395, 657
Gupta, A., Galeazzi, M., Koutroumpa, D., Smith, R., & Lallement, R. 2009, ApJ, 707, 644
Hagihara, T., Yao, Y., Yamasaki, N. Y., Mitsuda, K., Wang, Q. D., Takei, Y., Yoshino, T., & McCammon, D. 2010, PASJ, 62, 723
Hayashida, K., Inoue, H., Koyama, K., Awaki, H., & Takano, S. 1989, PASJ, 41, 373
Hoshino, A., et al. 2010, PASJ, 62, 371
Ishisaki, Y., et al. 2007, PASJ, 59, 113
Jaaniste, J., Tago, E., Einasto, M., Einasto, J., Andernach, H., & Mueller, V. 1998, A&A, 336, 35
Kaastra, J. S., Lieu, R., Tamura, T., Paerels, F. B. S., & den Herder, J. W. 2003, A&A, 397, 445
Kaastra, J. S., Mewe, R., & Nieuwenhuijzen, H. 1996, in UV and X-ray Spectroscopy of Astrophysical and Laboratory Plasmas, ed. K. Yamashita & T. Watanabe, 411–414
Kalberla, P. M. W., Burton, W. B., Hartmann, D., Arnal, E. M., Bajaja, E., Morras, R., & Pöppel, W. G. L. 2005, A&A, 440, 775
Kawaharada, M., et al. 2010, ApJ, 714, 423
Koyama, K., et al. 2007, PASJ, 59, 23
Kull, A., & Böhringer, H. 1999, A&A, 341, 23
Kushino, A., Ishisaki, Y., Morita, U., Yamasaki, N. Y., Ishida, M., Ohashi, T., & Ueda, Y. 2002, PASJ, 54, 327
Lumb, D. H., Warwick, R. S., Page, M., & De Luca, A. 2002, A&A, 389, 93
Mitsuda, K., et al. 2007, PASJ, 59, 1
Muñoz, J. A., & Loeb, A. 2008, MNRAS, 391, 1341
Narayanan, A., Savage, B. D., & Wakker, B. P. 2010a, ApJ, 712, 1443
Narayanan, A., Wakker, B. P., Savage, B. D., Keeney, B. A., Shull, J. M., Stocke, J. T., & Sembach, K. R. 2010b, ApJ, 721, 960
Ohashi, T., et al. 2010, in Society of Photo-Optical Instrumentation Engineers (SPIE) Conference Series, Vol. 7732, Society of Photo-Optical Instrumentation Engineers (SPIE) Conference Series
Piro, L., et al. 2009, Experimental Astronomy, 23, 67
Rossetti, M., & Molendi, S. 2010, A&A, 510, A83+
Sato, K., Kelley, R. L., Takei, Y., Tamura, T., Yamasaki, N. Y., Ohashi, T., Gupta, A., & Galeazzi, M. 2010, PASJ, 62, 1423
Schaye, J., et al. 2010, MNRAS, 402, 1536
Simionescu, A., et al. 2011, Science, 331, 1576
Smith, R. K., et al. 2007, PASJ, 59, 141
Takei, Y., Henry, J. P., Finoguenov, A., Mitsuda, K., Tamura, T., Fujimoto, R., & Briel, U. G. 2007a, ApJ, 655, 831
Takei, Y., et al. 2007b, PASJ, 59, 339
—. 2008, ApJ, 680, 1049
—. 2011, ApJ, 734, 91
Tawa, N., et al. 2008, PASJ, 60, 11
Tornatore, L., Borgani, S., Viel, M., & Springel, V. 2010, MNRAS, 402, 1911
Tripp, T. M., Bowen, D. V., Sembach, K. R., Jenkins, E. B., Savage, B. D., & Richter, P. 2006, in Astronomical Society of the Pacific Conference Series, Vol. 348, Astrophysics in the Far Ultraviolet: Five Years of Discovery with FUSE, ed. G. Sonneborn, H. W. Moos, & B.-G. Andersson, 341–+
Tripp, T. M., Sembach, K. R., Bowen, D. V., Savage, B. D., Jenkins, E. B., Lehner, N., & Richter, P. 2008, ApJS, 177, 39
Ursino, E., & Galeazzi, M. 2006, ApJ, 652, 1085
Ursino, E., Galeazzi, M., & Roncarelli, M. 2010, ApJ, 721, 46
Werner, N., Finoguenov, A., Kaastra, J. S., Simionescu, A., Dietrich, J. P., Vink, J., & Böhringer, H. 2008, A&A, 482, L29
Wiersma, R. P. C., Schaye, J., Dalla Vecchia, C., Booth, C. M., Theuns, T., & Aguirre, A. 2010, MNRAS, 409, 132
Wiersma, R. P. C., Schaye, J., & Theuns, T. 2011, MNRAS, 415, 353
Yoshino, T., et al. 2009, PASJ, 61, 805